# Multi-material Grayscale Stereolithography of Gradient Composites with Deterministic Control over Integration

*Archish Muralidharan, Asais Uzcategui, Robert McLeod* and Stephanie Bryant**

Prof. S. J. Bryant
Department of Chemical and Biological Engineering
University of Colorado, Boulder
Boulder, CO 80309, USA
Email: stephanie.bryant@colorado.edu

Prof. R. R. McLeod
Department of Electrical, Computer and Energy Engineering
University of Colorado, Boulder
Boulder, CO 80309, USA
Email: mcleod@colorado.edu

Prof. S. J. Bryant, Prof. R. R. McLeod
A. Muralidharan, A. C. Uzcategui
Materials Science and Engineering Program
University of Colorado, Boulder, USA
Boulder, CO 80309, USA

*Keywords: 3D printing, hydrogels, interface, diffusion, composites*

## ABSTRACT

3D printing enables integration of multiple materials with divergent properties through spatially patterned 3D-printed parts. While the spectrum of available materials affords large property variations, the interface between dissimilar materials is vulnerable to failure. The interface that forms between two materials is critical to the stability and function of a device. Hence, strategies are needed to predictably and precisely control integration. In this study, we explore integration of crosslinked polymers (hydrogels) for their widespread applications in 3D printing. The objectives were to establish a link between printing parameters to material properties to enable deterministic spatial control over integration via diffusion processes. By characterizing polymerization kinetics and mapping conversion to effective dose, it is possible to link printing parameters of light intensity and exposure time directly to conversion and ultimately to material properties of the printed resin. Applying this approach to grayscale exposures enabled spatial control over polymer mesh size, which then controls diffusion of the precursors of a second material. By precisely prescribing material properties, we demonstrate controlled integration of two heterogenous materials of different stiffness with interfacial regions that range from 10s of microns to millimeters, spatial defined patterns of integration and extended to layer-by-layer 3D printing using stereolithography.

Devices employed in biomedical,[1,2] soft electronics,[3] opto-electronics[4] and robotics[5,6] must often integrate soft functional materials with stiffer structural components. Integrating a broad spectrum of available materials affords large variations in properties with multiple functionalities to meet the demands of many applications.[7–9] However, the interface across dissimilar materials is vulnerable to mechanical failure.[10,11] Moreover, applications that use hydrated polymeric materials, such as hydrogels, are faced with the added challenge of differential swelling between heterogenous materials. This behavior introduces residual stresses and creates points of failure. Consequently, application of soft functional materials in devices demands improved methods to create robust interfaces between materials with strongly contrasting mechanical properties and/or swelling behavior.[12–14]

The interface that forms between the two materials is critical to the stability and function of a device. Although adhesives are efficient at bonding stiff materials together (e.g., metal implants to bone via bone cement) and separately soft materials together (e.g., soft tissues via fibrin glue), they are inadequate for heterogenous materials where stress concentrations develop.[15] An alternative to adhesives is to create a gradient across the interface to reduce stress concentrations and ensure structural integrity.[16–18] Nature has developed elegant solutions to overcome the mismatch in properties across heterogeneous tissues and reduce failure. For example, squid beaks have a soft base that gradually transitions to a hard tip by modulating the amount of water, chitin and proteins.[19] Teeth exhibit a gradual transition in composition at the dentino-enamel junction to dissipate load during mastication.[20] Examples of abrupt transitions also exist. For example, soft hyaline cartilage in articulating joints transitions abruptly to stiff calcified cartilage and the underlying subchondral bone.[21]

There is a need to develop engineering solutions that can predictably control the interface and, depending on the function of the device, prescribe programmable interfacial regions between two materials.[22,23] Gradients across an interfacial region have been achieved using sliding or grayscale photomasks[24,25] and microfluidic platforms.[26,27] Unfortunately, these approaches are inadequate for complex three-dimensional (3D) geometries that require overhanging features. 3D printing offers design flexibility to manufacture complex 3D devices with materials of divergent properties. However, the integration of multiple materials within a 3D printed device has been largely overlooked. For example, direct-ink writing-based 3D printing, which has become popular in biological applications, can produce composite materials with gradients, but its relatively low resolution (>100μm) prevents precise control over the interface.[28] Contrarily, stereolithography (SLA)-based 3D printing can produce complex and overhanging structures with high resolution (<20μm).[29,30] Recently, several studies have utilized SLA-based printing to fabricate materials with spatially varying crosslinking density.[31,32] Notably, a functionally graded soft robot body reduced mechanical failure during operation and improved performance.[33]

In this work, we demonstrate precisely prescribed 3D material properties to control interfaces between two materials with differing stiffness. In our approach, a 3D printed structure is polymerized using SLA, followed by a second process that introduces a second polymerizable material. Taking advantage of the spatial control afforded by SLA, precise grayscale illumination with a light resolution of 5 μm controls conversion during the printing process to yield a 3D printed part with spatially tuned crosslink density. The local crosslink density and swelling properties define the mesh size of the crosslinked network, which controls transport of the second material into the 3D printed part and creates a pre-defined region for integration between two materials. The two-stage photopolymerization process is depicted in **Figure 1**. The objectives for this study

were two-fold. The first objective establishes a link between polymerization kinetics, defined by the printing parameters (i.e., dose), and the resultant material properties (e.g., mesh size) to predictively prescribe regions of integration between two materials. The second objective demonstrates deterministic and spatial control over integration between two materials and applies it to 3D printing in SLA. We demonstrate interfacial regions that span from 50μm to over 1mm and which are straight, jagged, or spatially patterned. Such printable composites with tunable interfaces have the potential to revolutionize additive manufacturing.

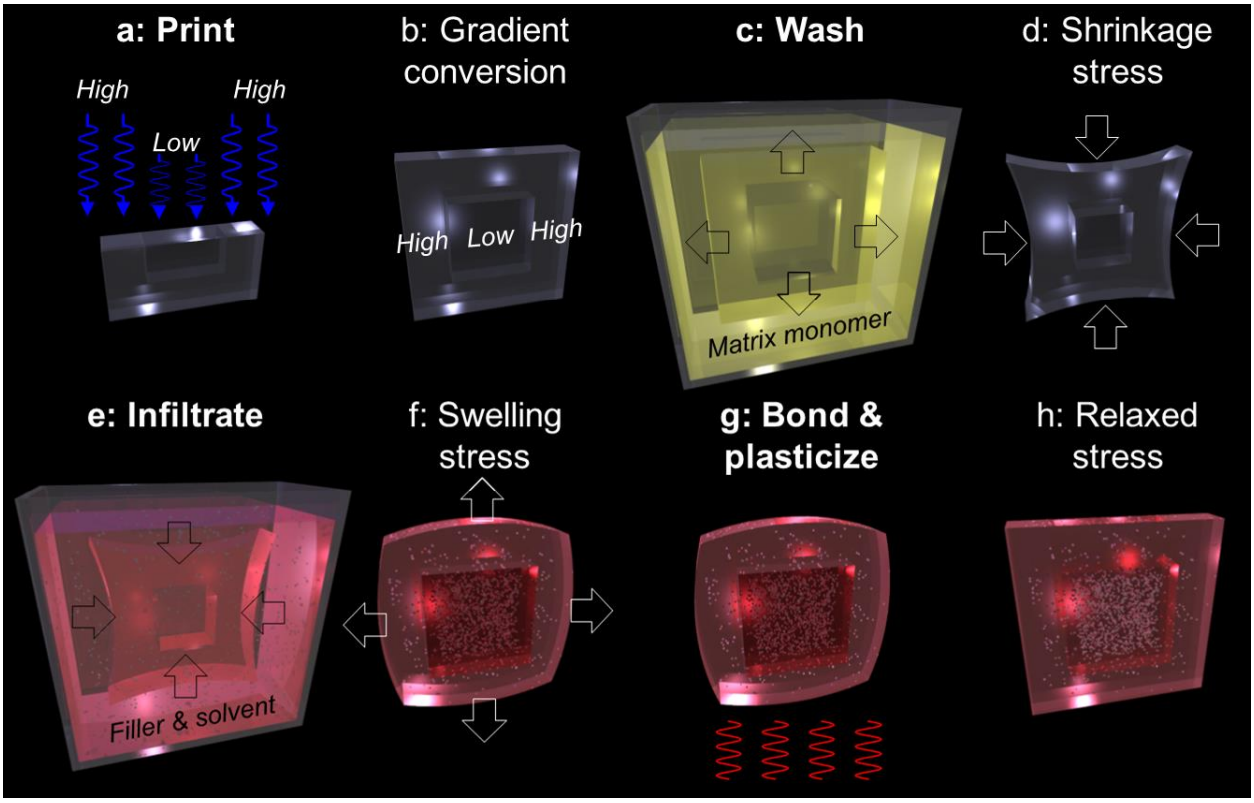


**Figure 1.** *Process overview for controlled integration of two materials. a,b)Grayscale patterning of material #1 resin followed by (c) solvent wash leads to spatially variable conversion of the resin monomer to (d) polymer. A soak in precursors for material #2 (e,f) results in selective diffusion into material#1 dictated by the local crosslink density which controls the mesh size. A flood cure (g,h) locks in material #2. This process can be extended to any pattern of desired integration.*

## 2. MATERIALS AND METHODS

**2.1 Materials.** Poly(ethylene glycol) diacrylate (PEGDA, MW=700Da), a tetrafucntional thiol, pentaerythritol tetrakis(3-mercaptopropionate) (PETMP), the photointitator, diphenyl(2,4,6-trimethylbenzoyl) phosphine oxide (TPO), poly(ethylene glycol) dithiol (PEGdt, MW=1 kDa) were purchased from Sigma-Aldrich. The 8-arm PEG-amine (MW= 10 kDa) was purchased from JenKem USA. The photoinitiator, I2959, was obtained from BASF. PolyFluor 570, Methacryloxyethyl thiocarbamoyl rhodamine B was obtained from Polysciences Inc. AlexaFluor 488 C5 Maleimide was obtained from ThermoFisher Scientific. AlexaFluor 488 Carboxylic Acid, 2,3,5,6-Tetrafluorophenyl Ester, 5-isomer was obtained from ThermoFisher Scientific. Phosphate buffered saline (PBS) was obtained from Corning. 2-(1H-7-azabenzotriazol-1-yl)-1,1,3,3-tetramethyluronium hexafluorophosphate methanaminium (HATU) was purchased from AK Scientific Inc. N,N-diisopropylethylamine (DIPEA), Dimethylformamide (DMF) and Dichloromethane (DCM) were purchased from Sigma-Aldrich

**2.2 Material Preparation.** Material #1 was formed from neat PEGDA 700Da (98.95wt%) and PETMP (1wt%) with TPO as the photoinitiator (0.05wt%). Free-radical polymerization was initiated using 405nm light at prescribed intensities between 6.25 mW/cm$^2$ to 50 mW/cm$^2$. Fluorescent material #1 was formed by adding 0.1mM rhodamine methacrylate to the precursor solution. Material #2 was formed from 8-arm poly(ethylene glycol) (10k Da) endcapped with norbornene (5wt%) (PEGNB) and PEGdt (stoichiometric ratio of 1 thiol to 1 ene) in PBS, I2959 as the photoinitiator (0.05wt%) at 25 mW/cm$^2$ using a 320-500nm light for 3 minutes. Briefly, PEGNB was synthesized from 8-arm PEGamine that was reacted overnight, at room temperature under inert atmosphere with 5-norbornene-2-carboxylic acid with HATU and DIPEA in DMF/DCM. The PEGNB product was precipitated in diethylether and then filtered, dialyzed and

lyophilized. Fluorescent monomers for material #2 were prepared by using AlexaFluor 488 C5 Maleimide (0.01 mM) for the PEGdt or AlexaFluor 488 TFP ester (0.01mM) for PEGNB. Fourier Transform Infrared Spectroscopy (FTIR) equipped for simultaneous light irradiation was used to monitor real-time conversion in material #1.

**2.3 Material Property Characterization.** The compressive modulus and swelling ratios were measured at different light intensity and exposure times. Hydrogels swollen to equilibrium in PBS were subjected to unconfined compression at a constant strain rate of 0.02mm/s with a 250 N load cell. The modulus reported is the slope of the stress vs strain curve between 10% and 15% strain. The equilibrium volumetric swelling ratios were determined from the equilibrium swollen mass, dry polymer mass after lyophilization, and the densities of the polymer and solvent. Crosslinking density, $\rho_x$ and polymer-solvent interaction parameter, $\chi_{12}$ were determined following methods described elsewhere that combine Flory-Rehner theory with theories of mixture and poroelasticity. The mesh size was estimated following Canal and Peppas,

$$\xi = Q^{1/3} C_n^{1/2} n^{1/2} l \quad (1)$$

where $Q$ is the equilibrium volumetric swelling ratio, $C_n$ is the characteristic ratio of the polymer assumed to be 4, $l$ is the average bond length assumed to be 1.54Å and $n$ is the number of bonds between crosslinks, which was determined from the crosslinking density.

**2.4 Imaging of composite materials.** Patterned material #1 was soaked in 70% Ethanol for 48hours followed by equilibrium swelling in di$H_2O$ or PBS. Depending on the experiment, the precursor solution for material #2 was introduced either into one side of the reservoirs in the 1D experiment or by submerging the material #1 in the precursor solution of material #2. The samples submerged were later photopolymerized to lock the material #2 in place. The composite samples

were swelled to equilibrium in di$H_2O$ and then imaged. Images were acquired using confocal microscopy (Zeiss LSM5 Pascal system) with a water immersed 10X objective lens. NIH ImageJ software was used to determine distances of overlapping fluorescence. Image J was also used to plot concentration profiles of fluorescence intensity as a function of distance into the gel. These profiles were fit to the solution of Fick's second law in 1-D to extract approximate diffusivities for the two conversions investigated.

**2.5 3D printing overhanging structures using SLA.** A custom-built projection SLA system equipped with a LED (λ=405nm, SOLIS-405C, Thorlabs) light source and spatial light modulator (1920x1152 Analog SLM, Meadowlark Optics) as the dynamic photomask was used. The optical resolution on the sample plane is 5μm. PEGDA 700 and PETMP were mixed at 99:1 wt% with 0.25 wt% TPO as a photoinitiator, 0.8 wt% Tinuvin1 CarboProtect1 as a photoabsorber and 0.05 wt% AIBN as a thermal initiator. The CAD design was composed of 200 μm diameter pillar structures connected by a lattice on top and bottom. The structures were soaked in 100% ethanol after 3D printing 1-2 min followed by placing in an oven at a temperature 105 +/-5 °C under vacuum for 1 h. Each construct was subsequently soaked in 70% ethanol for 24hr.

## 3. RESULTS AND DISCUSSION

**3.1 Hydrogel Chemistry and Resulting Stiffness.** We investigated integration between two photopolymerizable "ene" based poly(ethylene glycol) hydrogel materials of starkly different properties (Figure 2a). The stiff material was prepared from a neat solution of poly(ethylene glycol) diacrylate [PEGDA700] with 1% of four-arm thiol monomer [pentaerythritol tetrakis(3-mercaptopropionate), PETMP], which was added to decrease oxygen inhibition time.[34] PETMP decreases polymerization time and introduces additional crosslink points to enhance stiffness.[35]

An acrylate-based resin was selected for its wide use in additive manufacturing. The soft material was prepared from reacting 8-arm PEG (10 kDa, 5wt%) functionalized with norbornene (PEGNB) and a PEG dithiol (1 kDa, PEGdt) crosslinker. A light activated thiol-norbornene resin was selected due to its promise in biological applications, minimal side products and demonstrated cytocompatibility and biocompatibility.[36,37] At complete conversion, the stiff and soft hydrogel yielded a modulus of 40 (2) MPa and 54 (9) kPa, respectively, [mean (standard deviation)] (Figure 2a). In this work, we 3D print the stiff hydrogel as material #1 and then backfill with the soft hydrogel as material #2.

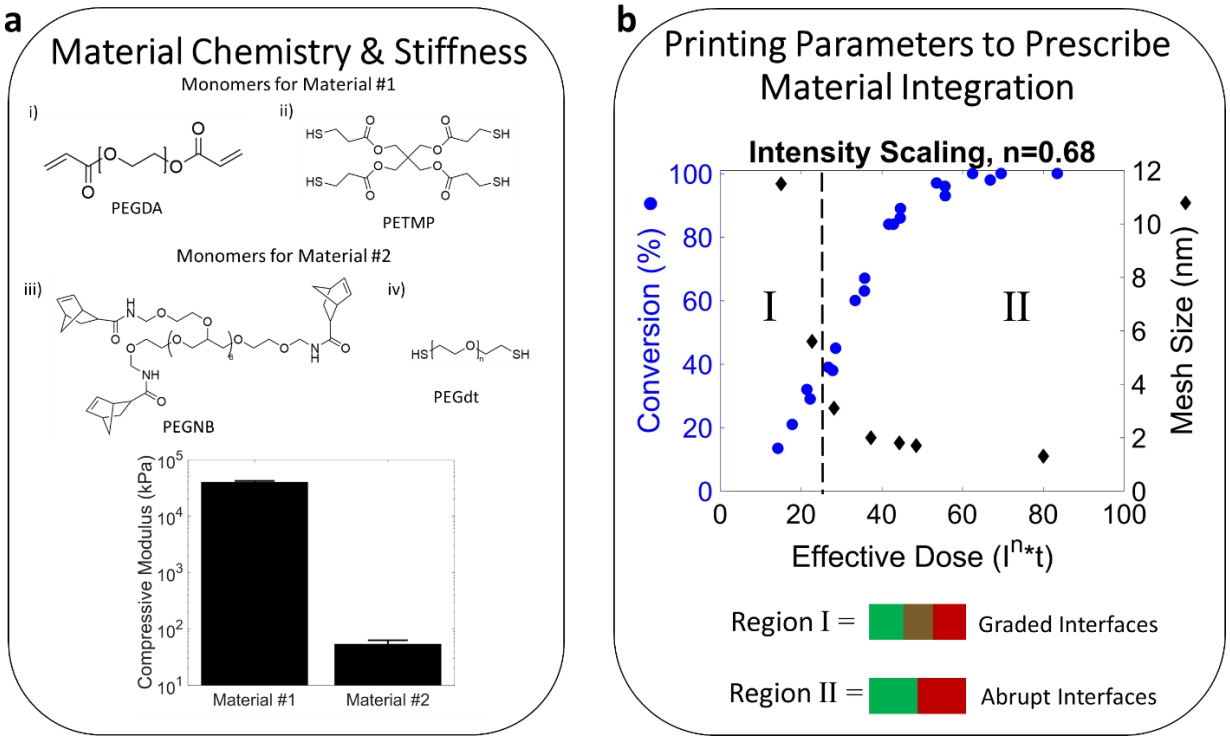


**Figure 2.** *a) Chemical structures of monomers used in this study for both materials #1 and #2 and their corresponding compressive moduli. b) Conversion for material #1 and the corresponding mesh size of material #1 as a function of an effective dose. When in region I, the mesh size of material #1 is larger than the size of diffusing monomers of material #2 enabling their transport and integration. When in region II, the mesh size of material #1 is smaller than the diffusing monomers and hence transport and integration is inhibited, and instead a sharp interface forms.*

**3.2 Correlating Material Property to Printing Parameters.** Grayscale illumination offers a facile mechanism to spatially control the local properties at the interface relative to the bulk properties of the part. We begin by deriving a relationship between SLA printing parameters of light intensity and exposure time (i.e., exposure dose), which is precisely controlled by grayscale illumination, and conversion of the polymerizing species (i.e., material #1). We then establish a correlation between conversion and the resulting material properties such that grayscale illumination can be used to predictably define the material properties in space.

The reaction of material #1, used for 3D printing, was characterized by FTIR at various intensities and exposure times. The rate of polymerization ($R_p$) is related to the rate of initiation ($R_i$), which is in turn related to the incident light intensity ($I_o$) and initiator concentration ($[In]$) through the steady state approximation given by the power law relationship:

$$R_p \approx R_i^{\alpha} \approx (I_o[In])^{\alpha} \quad (2)$$

Accounting for the three distinct events of oxygen inhibition, light-induced polymerization, and dark polymerization,[38] the scaling factor, α was determined to be 0.68 (0.01).[39] With this scaling factor, conversion as a function of effective dose ($I_o^{\alpha}$ x time) reduces to a single master curve (Figure 2b). From this curve, conversion is predicted at any intensity and time for material #1.

To correlate conversion to material properties, compressive modulus *E*, equilibrium swelling ratio *Q*, and mesh size ξ for material #1 were measured at discrete conversions. At 13.5% conversion, E and *Q* were 1 (0.08) MPa and 5.7 (0.36), respectively. At complete (i.e., ~100%) conversion, *E* and *Q* were 40 (2) MPa and 1.6 (0.01), respectively. The mesh size was estimated from *E* and *Q* and ranged from 1.3 nm (at 100% conversion) to 11.5 nm (at 13.5% conversion). We confirmed that for a given effective dose, the resulting material properties of material #1 do

not vary significantly with light intensity. When combined, the mesh size of material #1 can be prescribed by effective dose (Figure 2b).

**3.3 Characterization of Diffusive Transport of Material #2 Precursors into Bulk Printed Material #1.** To enable regions of integration to be predictably prescribed, we next characterized diffusion of the monomers for material #2 into a bulk printed material #1. The latter was prepared at two effective doses, one yielding partial conversion and hence large mesh size and one yielding complete conversion and hence small mesh size. Using a 1D experimental set-up (**Figure 3**a) with material #1 swollen to equilibrium and fluorescently labeled (red), diffusion of each monomer labeled with a green fluorophore was monitored in time and space. For the fully converted (~100%) case, there was no diffusion of 8-arm PEGNB or PEGdt monomer observed into material #1 evident by a lack of change in the green fluorescence intensity profile as a function of distance from 0 to 24hrs (Figure 3b,3c). This result is supported by estimates of a 1.3 nm mesh size and hydrodynamic radii for PEGdt and PEGNB at 2.3 and 4.7 nm, respectively. Thus, at full conversion, monomers of material #2 are too large to diffuse into material #1 and their interaction is limited to the surface of material #1. For the partially converted (13.5%) case, the 11.5 nm mesh size is substantially larger and PEGNB (Figure 3d) and PEGdt (Figure 3e) monomers diffuse through the network. The PEGNB transport is consistent with Fickian diffusion with a diffusivity, $D$, estimated to be $25 \times 10^{-8}$ $cm^2/s$. Contrarily, transport of PEGdt is characteristic of a reaction-diffusion mechanism, where the concentration of PEGdt in the network is higher than in the reservoir solution. This occurs as thiols from PEGdt react with pendant acrylates in material #1 via the Michael-type addition reaction.[40] The reaction-diffusion mechanism was confirmed by monitoring diffusion of fluorophore-labeled PEG (1kDa) (Figure 3f), which showed a concentration profile consistent with Fickian diffusion and a diffusivity of $72 \times 10^{-8}$ $cm^2/s$. By

controlling the mesh size of material #1 and the reactivities of materials #1 and #2, it is possible to selectively prescribe the distance over which integration is possible from a sharp interface (Region *II*), where diffusion is limited, to a wide interfacial region (Region *I*) where diffusion can occur (Figure 2b).

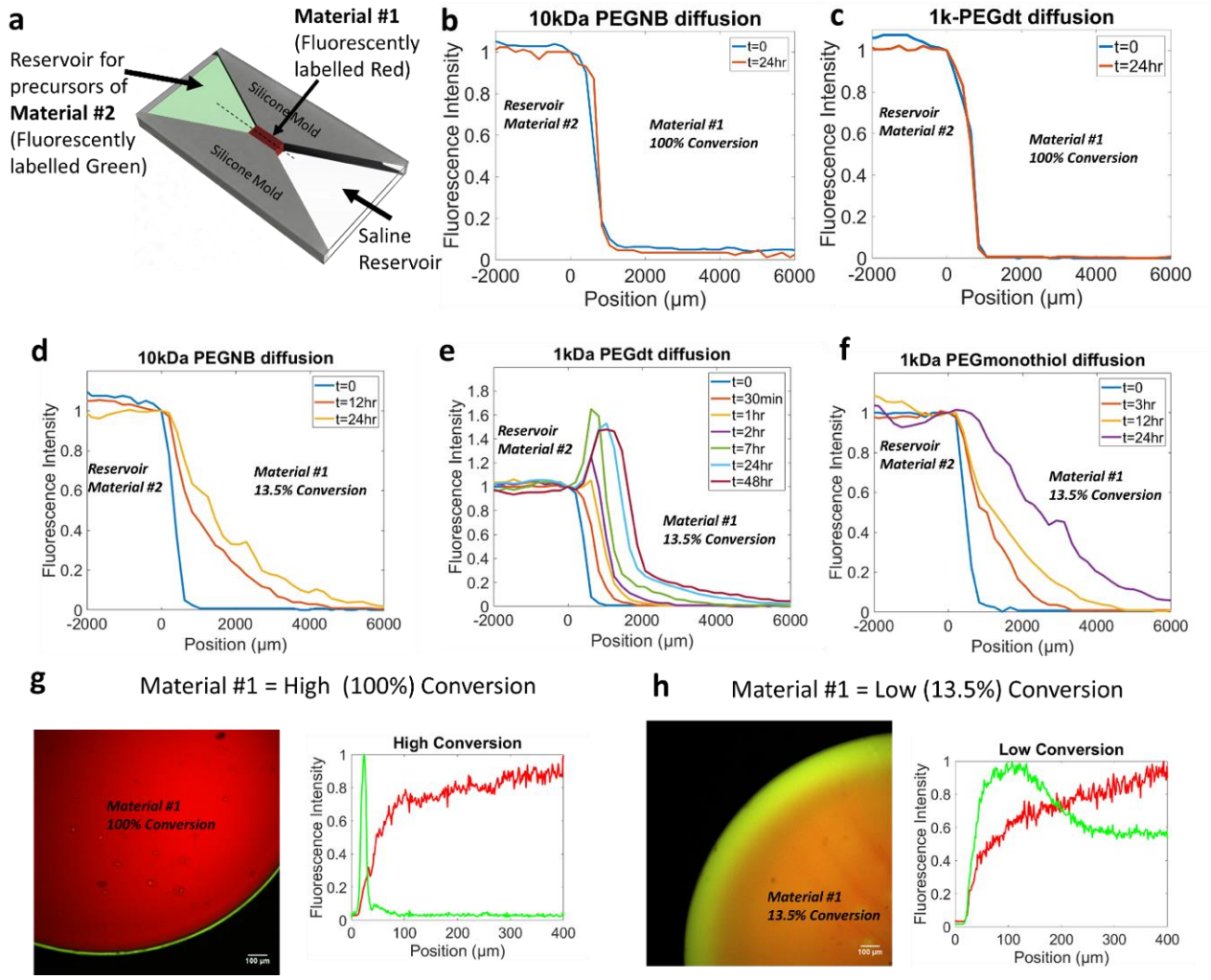


**Figure 3.** *Characterization of one-dimensional diffusion of each monomer fluorescently labeled green for material #2 into a bulk printed material #1 fluorescently labeled red as a function of time. a) Schematic of experimental setup. Diffusion of monomers b) 10k PEGNB and c) 1k PEGdt into material #1 at ~100% conversion shows no transport. Diffusion of d) 10k PEGNB, e) 1k PEGdt, and f) 1k PEGmonothiol into material #1 at 13.5% conversion shows transport. The in-diffusing PEGdt reacts with pendant acrylate groups in material #1 via Michael addition mechanism leading to reaction-diffusion transport whereas with 1k PEG with no free thiols is consistent with Fickian diffusion. Representative confocal microscopy images and corresponding line scan profile along the edge of material #1 surface shows a sharp interface (g) vs two*

*integrated materials (h) after diffusion of material #2 monomers into material #1 followed by a flood cure.*

These experiments were extended to include a second photopolymerization to lock material #2 in place following the in-diffusion step. Monomers from material #2 were allowed to diffuse into material #1 for an extended time (48 hours). When material #1 was fully (~100%) converted, a sharp interface is observed (Figure 3g). Contrarily, when material #1 was partially converted (13.5%), material #2 was integrated across the entire material #1 (Figure 3h). Upon the second polymerization, material #2 forms an interpenetrating network along with covalent bonds to material #1 through free acrylates and thiols.

**3.4 Demonstration of Deterministic Spatial Control over Integration.** These results were used to design a grayscale illumination pattern to demonstrate deterministic control of variable conversion in a 3D printed part for controlled integration. We harnessed spatial control of the local properties of material #1 to direct monomer transport of material #2 into pre-defined regions of the printed matrix. Material #1 was patterned with an inner core that was prescribed at full conversion (i.e., ~100%) and an outer shell that was prescribed at partial conversion (13.5%). The shell was designed to permit transport and integration of material #2 while the core was designed to prevent transport. At extended diffusion times, the shell represents the region of integration. The shell width, and hence integration distance, was patterned from 50μm to 500μm (**Figure 4**a-e). The distance over which material #2, after in-diffusing for 48 hours and photopolymerized, integrated into material #1 directly correlated to the prescribed shell pattern. Through simple spatial control over conversion, the distance of integration is readily tunable. This approach demonstrates that composite materials with pre-defined interfaces can be created on demand.

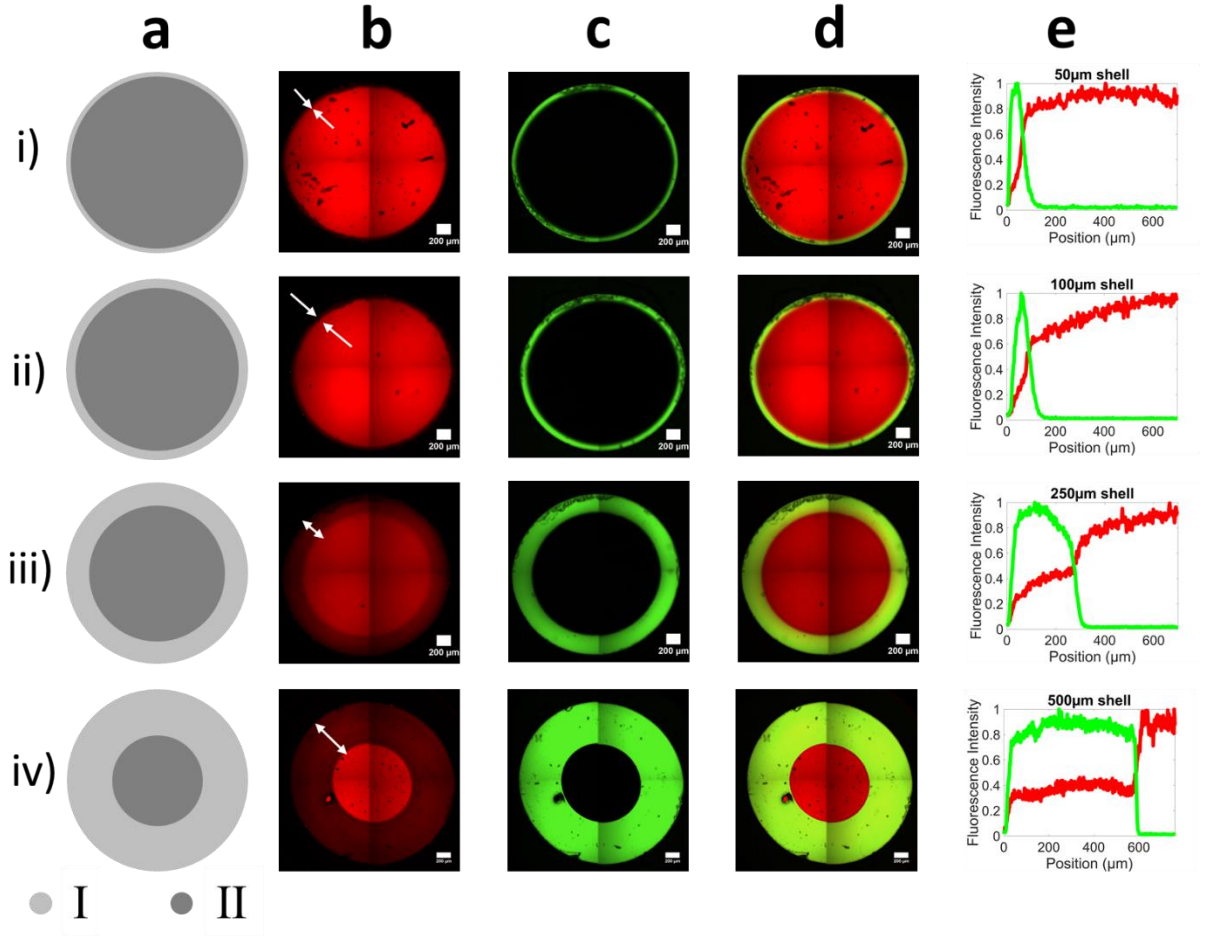


**Figure 4.** *Grayscale illumination to spatially control the local properties of material #1 (red) to control integration of material #2 (green). a) Digital projected image of illumination pattern showing a core at high (~100%) and a shell at low (13.5%) conversion. Region I shell thickness is 50 μm in (i),100 μm in (ii), 250μm in (iii) and 500 μm in (iv) for a 2 mm cylinder. Representative confocal microscopy images of b) Material #1, c) Material #2, and d) the composite image. Representative confocal microscopy images stitched from four images of the composite material recapitulates the digital image. e) Line profiles of each fluorescence intensity across the integration region. In all cases, no integration is observed in the core.*

**3.5 Characterization of the Failure of a Composite Material with Different Interfacial Properties.** We probed the failure point of a composite material comprised of these two heterogenous materials as a function of their integration when pulled under tension to failure (Figure 5a,5b).

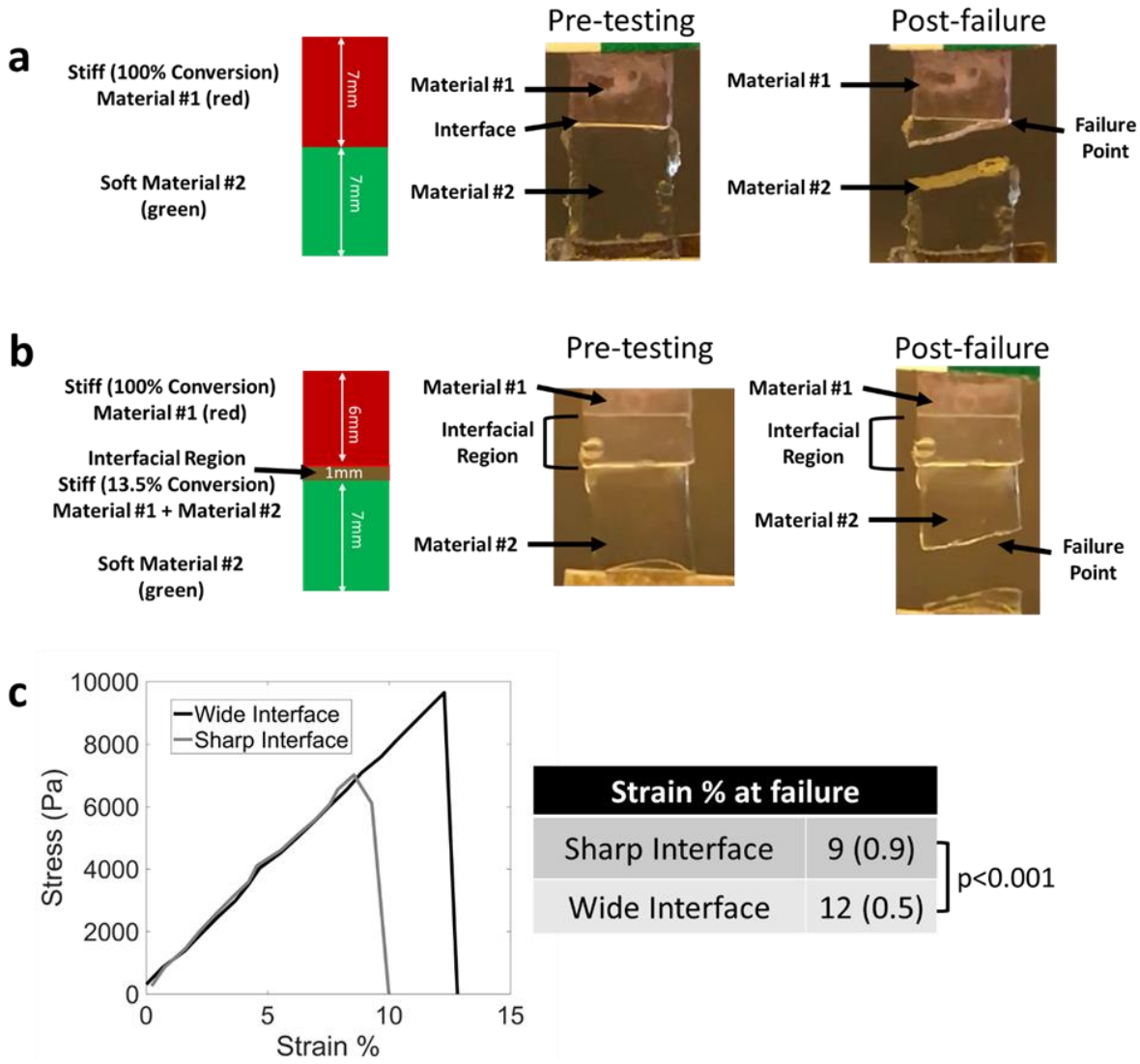


**Figure 5.** *Tensile tests were performed to failure for a composite material composed of material #1 and #2 with a sharp interface (a) and a programmed integrated region (b). Digital photographs are shown for a representative sample before and after failure. c) Stress vs Strain plot showing a higher strain to failure for the wide interface case (Data presented as mean and standard deviation for n=3-4).*

In one case, a rectangular sample was designed with a sharp interface consisting of a 7-mm in length material #1 photopolymerized to full (~100%) conversion followed by introducing material #2 and polymerizing to create a 14-mm long sample. In the second case, material #1 was patterned with a 6-mm long region at full (~100%) conversion adjacent to a 1-mm long region at partial (13.5%) conversion. The second material was introduced, in-diffused for 48 hours, and

photopolymerized to create 14-mm long sample. In the first case, the failure of the composite material occurred at the interface (Figure 5a). In the second case, failure of the composite material occurred in the soft material #2 (Figure 5b). Representative tensile stress vs stain plot for the composite material with sharp and wide interface (Figure 5c), shows that the wider interface has a higher strain to failure and the failure occurs completely in the soft hydrogel. The results quantitatively demonstrate that a prescribed interfacial region that interlocks the two heterogenous materials lead to enhanced mechanical robustness across the interface.

**3.6 Demonstration of Patterned Integration with Complex Contours and Jagged Features.** In the next series of experiments, we illustrate the potential of this approach to deterministically control site-specific integration in arbitrary patterns. In our first example, we were inspired by the wavy tide mark at the osteochondral interface between the deep zone of cartilage and calcified cartilage. To imitate this tide mark, we patterned a jagged interface between fully and partially converted regions of material #1, followed by in-diffusion and polymerization of material #2. The grayscale patterns were recapitulated in the hydrogel with high fidelity (**Figure 6**a). Extending this idea, patterns of alternating high and low conversion regions and patterns of high and low regions intermixed into arbitrary patterns demonstrate excellent fidelity of spatial control (Figure 6b). For example, in the same hydrogel construct we show that material #2 was localized to a low conversion channel (200-μm width and 2-mm in length) embedded in a high conversion matrix, but in a different region was inhibited in areas of high conversion that were in the shape of triangles embedded in a low conversion matrix. Furthermore, a pattern of the CU buffalo logo with spatially varied crosslinking density demonstrates preferential placement of material #2 to form the letters ‘CU’ (Figure 6c).

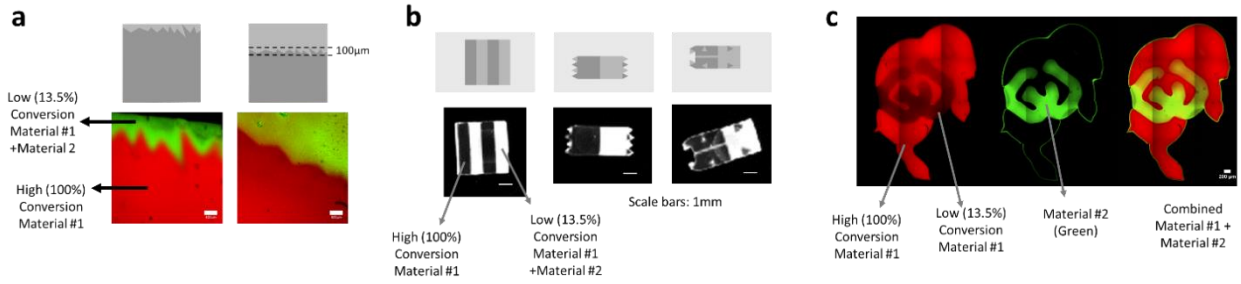


**Figure 6.** *Illustrations of controlled integration in 3D composite materials composed of material #1 and #2 with very different stiffness (see Figure 2a). In all examples, grayscale digital projected images are shown followed by the resulting composite material. Examples include a) a jagged interface with a small (left) or large (right) region of integration region, b) undulating boundaries and site-specific integration, c) site-specific integration with high fidelity with the letters 'CU' in a patterned CU Buffalo logo*

### 3.7 Demonstration of Deterministic 3D control over Integration in 3D Printed Parts by SLA.

A 3D scaffold with infilled soft hydrogel was implanted into a rabbit knee to promote cartilage formation and prevent the bony bar formation in its place. Figure 7a shows an SEM image of the scaffold and the X-Ray microscope image of the scaffold after 8 weeks of implantation in a rabbit knee (Figure 7a). 3D X-Ray images at 2 different angles confirm that there the composite scaffold has prevented the bony bar formation after 8 weeks of implantation (Figure 7b).

Finally, to demonstrate control over integration in 3D, material #1 was printed using SLA and then backfilled with material #2. In this example, layer-by-layer printing was used to form two uniform platforms of 125-μm thickness separated by cylindrical pillars of 200-μm diameter and 1.25-mm height (Figure 7c). Two cases are shown to demonstrate control over integration in 3D (Figure 7). In the first, the exposure dose was uniform across the 200-μm printed pillars (Figure 7d,e,f). In the second, the pillars were printed with a 100-μm diameter high conversion core and 50-μm low conversion outer shell (Figure 7g,h,i). In both cases, in-diffusion of monomers of material #2 was followed by polymerization of material #2. The results demonstrate the ability to achieve a sharp

interface or wide (~100 µm) interfacial region between two materials spanning three-orders of magnitude in stiffness (40 MPa for material #1 and 53 kPa for material #2) within a single 3D printed part.

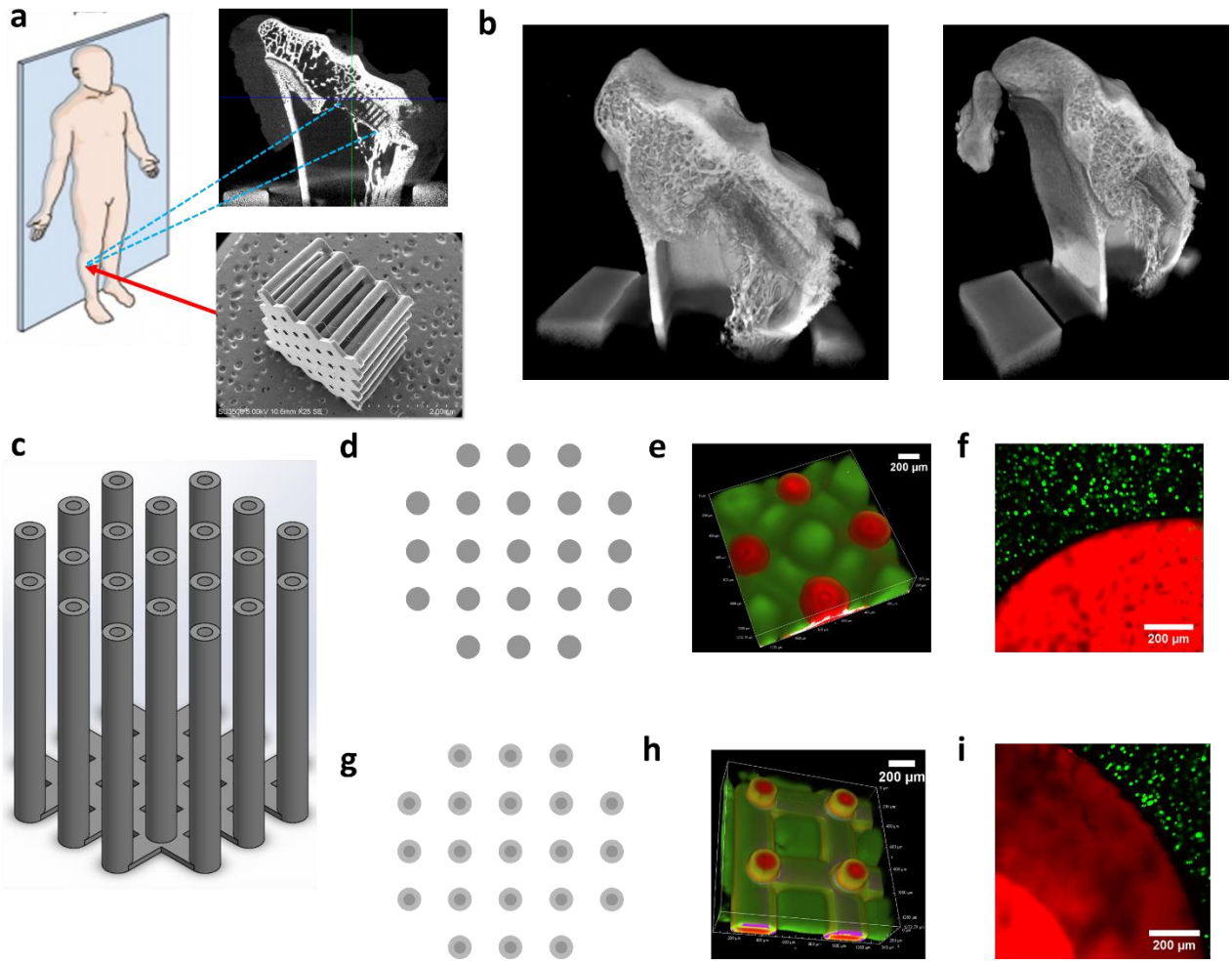


**Figure 7.** *a) A 3D printed stiff scaffold structure with soft infilled hydrogel implanted in a rabbit knee. b) 3D X-Ray microscope images at two different angles shows the implant prevents bony bar formation. c) The scaffold includes a lattice base off of which pillars each with a diameter of 200µm, were patterned with material #1 either at high (100%) conversion (d,e,f) or with a 50µm shell of low (13.5%) conversion (g,h,i) shown by grayscale digital projected image, and confocal microscopy images, confocal microscopy images of scaffolds with MC3T3 cells embedded in the soft hydrogel.*

## 4. CONCLUSIONS

In summary, we developed a highly adaptable and tunable approach that enables precise control over the integration of two heterogenous crosslinked polymeric materials in 3D printed parts formed from SLA. We demonstrate spatial control over the integration enabling coupling of two materials over distinct regions or across the interface. The versatility of this process creates the possibility to integrate materials with varying properties in 3D space. With the flexibility afforded by SLA, our approach can readily be extended to a variety of crosslinked polymeric materials with complex geometries and pave the way for new generation of materials with highly contrasting properties within the same device.

**Acknowledgments**

The authors would like to thank Dr. Karin Payne and Dr. Yangyi Yu for performing the in vivo studies in rabbit model. Research reported in this publication was supported by the National Institute of Arthritis and Musculoskeletal and Skin Diseases of the National Institute of Health under Award Numbers 1R01AR069060, by the National Institute of Child Health and Human Development of the NIH under Award Number 1R21HD090696 and by the National Science Foundation under Grant Number 1826454.

## 5. REFERENCES

[1] T. Lühmann, H. Hall, *Materials* **2009**, *2*, 1058.
[2] E. A. Aisenbrey, A. Tomaschke, E. Kleinjan, A. Muralidharan, C. Pascual-Garrido, R. R. McLeod, V. L. Ferguson, S. J. Bryant, *Macromol. Biosci.* **n.d.**, *18*, 1700267.
[3] Z. Zhu, D. Ju, Y. Zou, Y. Dong, L. Luo, T. Zhang, D. Shan, H. Zeng, *ACS Appl. Mater. Interfaces* **2017**, *9*, 12092.
[4] Y. Meng, M. Tsai, G. R. Schmidt, M. Anthamatten, *ACS Appl. Mater. Interfaces* **2015**, *7*, 8601.
[5] R. Luo, J. Wu, N.-D. Dinh, C.-H. Chen, *Adv. Funct. Mater.* **n.d.**, *25*, 7272.
[6] A. Miriyev, K. Stack, H. Lipson, *Nat. Commun.* **2017**, *8*, 596.
[7] J. Mueller, J. R. Raney, K. Shea, J. A. Lewis, *Adv. Mater.* **2018**, *30*, 1705001.

[8] J. Odent, T. J. Wallin, W. Pan, K. Kruemplestaedter, R. F. Shepherd, E. P. Giannelis, *Adv. Funct. Mater.* **2017**, *27*, 1701807.
[9] X. Kuang, K. Chen, C. K. Dunn, J. Wu, V. C. F. Li, H. J. Qi, *ACS Appl. Mater. Interfaces* **2018**, *10*, 7381.
[10] H. Li, Y. J. Tan, K. F. Leong, L. Li, *ACS Appl. Mater. Interfaces* **2017**, *9*, 20086.
[11] D. Kokkinis, F. Bouville, A. R. Studart, *Adv. Mater.* **2018**, *30*, 1705808.
[12] A. Sola, D. Bellucci, V. Cannillo, *Biotechnol. Adv.* **2016**, *34*, 504.
[13] S. H. Park, R. Su, J. Jeong, S.-Z. Guo, K. Qiu, D. Joung, F. Meng, M. C. McAlpine, *Adv. Mater.* **n.d.**, *0*, 1803980.
[14] R. Libanori, R. M. Erb, A. Reiser, H. Le Ferrand, M. J. Süess, R. Spolenak, A. R. Studart, *Nat. Commun.* **2012**, *3*, 1265.
[15] B. A. Harley, A. K. Lynn, Z. Wissner-Gross, W. Bonfield, I. V. Yannas, L. J. Gibson, *J. Biomed. Mater. Res. A* **2010**, *92*, 1078.
[16] K. U. Claussen, R. Giesa, H.-W. Schmidt, *Polymer* **2014**, *55*, 29.
[17] J. A. Neal, N. J. Oldenhuis, A. L. Novitsky, E. M. Samson, W. J. Thrift, R. Ragan, Z. Guan, *Angew. Chem. Int. Ed.* **2017**, *56*, 15575.
[18] N. Naserifar, P. R. LeDuc, G. K. Fedder, *Adv. Mater.* **n.d.**, *28*, 3584.
[19] A. Miserez, T. Schneberk, C. Sun, F. W. Zok, J. H. Waite, *Science* **2008**, *319*, 1816.
[20] P. Zaslansky, A. A. Friesem, S. Weiner, *J. Struct. Biol.* **2006**, *153*, 188.
[21] B. L. Banik, D. T. Bowers, P. Fattahi, J. L. Brown, in *Bio-Instr. Scaffolds Musculoskelet. Tissue Eng. Regen. Med.*, Academic Press, **2017**, pp. 203–233.
[22] F. Hanßke, O. Bas, C. Vaquette, G. Hochleitner, J. Groll, E. Kemnitz, D. W. Hutmacher, H. G. Börner, *J. Mater. Chem. B* **2017**, *5*, 5037.
[23] W. Shi, A. L. Hamilton, K. T. Delaney, G. H. Fredrickson, E. J. Kramer, C. Ntaras, A. Avgeropoulos, N. A. Lynd, Q. Demassieux, C. Creton, *Macromolecules* **2015**, *48*, 5378.
[24] R. A. Marklein, J. A. Burdick, *Soft Matter* **2009**, *6*, 136.
[25] A. M. Kloxin, J. A. Benton, K. S. Anseth, *Biomaterials* **2010**, *31*, 1.
[26] J. He, Y. Du, J. L. Villa-Uribe, C. Hwang, D. Li, A. Khademhosseini, *Adv. Funct. Mater.* **2010**, *20*, 131.
[27] M. P. Cuchiara, A. C. B. Allen, T. M. Chen, J. S. Miller, J. L. West, *Biomaterials* **2010**, *31*, 5491.
[28] J. Perelaer, B.-J. de Gans, U. S. Schubert, *Adv. Mater.* **2006**, *18*, 2101.
[29] F. P. W. Melchels, J. Feijen, D. W. Grijpma, *Biomaterials* **2010**, *31*, 6121.
[30] J. Z. Manapat, Q. Chen, P. Ye, R. C. Advincula, *Macromol. Mater. Eng.* **2017**, *302*, 1600553.
[31] G. I. Peterson, J. J. Schwartz, D. Zhang, B. M. Weiss, M. A. Ganter, D. W. Storti, A. J. Boydston, *ACS Appl. Mater. Interfaces* **2016**, *8*, 29037.
[32] C. Xia, N. Fang, *J. Micromechanics Microengineering* **2009**, *19*, 115029.
[33] N. W. Bartlett, M. T. Tolley, J. T. B. Overvelde, J. C. Weaver, B. Mosadegh, K. Bertoldi, G. M. Whitesides, R. J. Wood, *Science* **2015**, *349*, 161.
[34] A. K. O'Brien, N. B. Cramer, C. N. Bowman, *J. Polym. Sci. Part Polym. Chem.* **2006**, *44*, 2007.
[35] A. E. Rydholm, N. L. Held, C. N. Bowman, K. S. Anseth, *Macromolecules* **2006**, *39*, 7882.
[36] L. D. Amer, S. J. Bryant, *Ann. Biomed. Eng.* **2016**, *44*, 1959.
[37] B. D. Fairbanks, M. P. Schwartz, A. E. Halevi, C. R. Nuttelman, C. N. Bowman, K. S. Anseth, *Adv. Mater.* **2009**, *21*, 5005.
[38] J. Pavlinec, N. Moszner, *J. Appl. Polym. Sci.* **2003**, *89*, 579.
[39] A. C. Uzcategui, A. Muralidharan, V. L. Ferguson, S. J. Bryant, R. R. McLeod, *Adv. Eng. Mater.* **n.d.**, *0*, DOI 10.1002/adem.201800876.
[40] D. P. Nair, M. Podgórski, S. Chatani, T. Gong, W. Xi, C. R. Fenoli, C. N. Bowman, *Chem. Mater.* **2014**, *26*, 724.